ARTICLES
https://doi.org/10.1038/s41565-020-00828-6
nature nanotechnology

Ultrafast hole spin qubit with gate-tunable spin–orbit switch functionality

Florian N. M. Froning[1,3], Leon C. Camenzind[1,3], Orson A. H. van der Molen[1,2], Ang Li[2], Erik P. A. M. Bakkers[2], Dominik M. Zumbühl[1]✉ and Floris R. Braakman[1]✉

Quantum computers promise to execute complex tasks exponentially faster than any possible classical computer, and thus spur breakthroughs in quantum chemistry, material science and machine learning. However, quantum computers require fast and selective control of large numbers of individual qubits while maintaining coherence. Qubits based on hole spins in one-dimensional germanium/silicon nanostructures are predicted to experience an exceptionally strong yet electrically tunable spin–orbit interaction, which allows us to optimize qubit performance by switching between distinct modes of ultrafast manipulation, long coherence and individual addressability. Here we used millivolt gate voltage changes to tune the Rabi frequency of a hole spin qubit in a germanium/silicon nanowire from 31 to 219 MHz, its driven coherence time between 7 and 59 ns, and its Landé *g*-factor from 0.83 to 1.27. We thus demonstrated spin–orbit switch functionality, with on/off ratios of roughly seven, which could be further increased through improved gate design. Finally, we used this control to optimize our qubit further and approach the strong driving regime, with spin-flipping times as short as ~1 ns.

Spin qubits defined in Si and Ge quantum dots are of particular interest for scaling-up quantum circuits due to their small size, speed of operation and compatibility with the semiconductor industry[1–4]. Both materials feature a low natural abundance of non-zero nuclear spins, which has led to the demonstration of long qubit coherence times[1,5,6], as well as single-qubit[6–8] and two-qubit[9–12] operations with high fidelity. Most of this research has been performed using electron spin states to define the qubit[13]. Hole spin qubits[4,14–16] have recently gained attention as they potentially enable faster quantum operations and a higher level of control over the qubit parameters[17–20]. In addition, hole spins in Ge and Si may have improved relaxation and decoherence times, as they do not exhibit a valley degeneracy and their wavefunction has reduced overlap with nuclear spins[21,22]. Importantly, spin–orbit interaction (SOI) can be exceptionally strong for hole spins in low-dimensional nanostructures[23,24], particularly in Ge- or Si-based nanowires[17,20]. This enables very fast spin control through electric dipole spin resonance (EDSR)[25–28], in which a time-varying electric field periodically displaces the hole wave function, and thus creates an effective periodic magnetic field through the SOI. In this way, EDSR can be used for all-electrical spin manipulation without requiring micromagnets[29] or coplanar striplines[30], which add to the device complexity.

Rabi frequencies of around 100 MHz have been measured for hole spins[12,31], but predictions for one-dimensional systems range even up to 5 GHz, made possible by the particularly strong direct Rashba SOI[17,19]. Conversely, this strong SOI may lead to an undesired enhancement of qubit relaxation and dephasing rates via coupling to phonons or charge noise. However, the direct Rashba SOI is also predicted to be tunable to a large extent through local electric fields[17,18,20], which enables electrical control over the SOI strength and the Landé *g*-factor. Such electrical tunability provides a path towards a spin qubit with a switchable interaction strength, using what we term a spin–orbit switch. The spin–orbit switch can be used to selectively idle a qubit in an isolated configuration of weak SOI and low decoherence (idle state), whereas for fast manipulation it is tuned into a regime of strong SOI (control state) and is selectively coupled to an EDSR driving field or microwave resonator by controlling the qubit Zeeman energy[19,32]. Here we experimentally realized the key components of this approach, through the demonstration of an ultrafast and electrically tunable hole spin qubit in a Ge/Si core/shell nanowire. We used SOI-mediated EDSR to perform fast two-axis qubit control and implement Ramsey and Hahn echo pulsing techniques to compare the qubit's coherence times. We then demonstrated a high degree of electrical control over the Rabi frequency, *g*-factor and driven qubit decay time by tuning the voltage on one of the dot-defining gates, which illustrates the basic ingredients of a spin–orbit switch. The spin–orbit switch functionality that we demonstrate here shows moderate on/off ratios of about seven for both Rabi frequency and coherence times, which in future devices could be increased through improved gate design. We extracted a spin–orbit length (l_{SO}) that was extraordinarily short and electrically tunable over a large range down to 4 nm for holes of heavy-hole mass. This control allowed us to optimize our qubit for speed of operation, which resulted in Rabi frequencies as large as 435 MHz.

Set-up and measurement techniques

Figure 1a shows a scanning electron micrograph of the device, which comprises five gates beneath a Ge/Si core/shell nanowire[33–35]. A depletion-mode few-hole double quantum dot was formed inside the nanowire by positively biasing the five bottom gates. Throughout this work, we performed measurements of electronic transport through the double quantum dot, using the source and drain contacts indicated in Fig. 1a (for more details about the device and measurement set-up, see Methods). We operated the device at a transition that exhibited Pauli spin blockade[36], which we used for spin readout in the transport measurements.

In our set-up, gates L and LP were connected via bias tees to high-frequency lines, as indicated in Fig. 1a, which allowed us to apply square voltage pulses and microwave bursts to these gates.

[1]University of Basel, Basel, Switzerland. [2]Department of Applied Physics, Eindhoven University of Technology, Eindhoven, the Netherlands. [3]These authors contributed equally: Florian N. M. Froning, Leon C. Camenzind. ✉e-mail: dominik.zumbuhl@unibas.ch; floris.braakman@unibas.ch

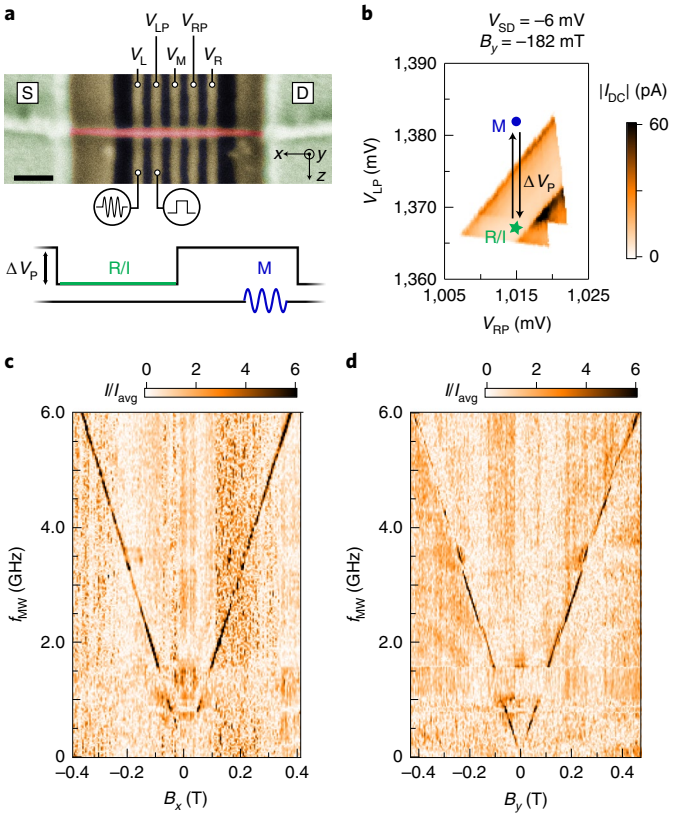

Fig. 1 | Experimental set-up and EDSR. a, Scanning electron micrograph of a cofabricated device showing the source (S) and drain (D) contacts and gates. Scale bar, 100 nm. Inset: illustration of the pulse scheme. The points R, I and M indicate the locations of the readout, initialization and manipulation stages, respectively, of the pulsing scheme (see **b**). The depth of the square pulse is ΔV_P. **b**, Measurement of a set of bias triangles taken with a source–drain voltage (V_{SD}) of −6 mV showing Pauli spin blockade, which is partially lifted at the finite magnetic field $B_y = -182$ mT. **c**,**d**, Spin-blockade leakage current, which shows EDSR as a function of f_{MW} and magnetic field magnitude in the x (**c**) and y (**d**) directions. Horizontal bands of decreased intensity are due to microwave resonances in the high-frequency circuitry. For detailed measurement parameters and description of the data analysis, see Methods.

The measurements were performed with a two-stage pulse scheme (Fig. 1a, inset). First, the system was initialized at point I (Fig. 1b) in a spin-blockaded triplet state. Then, with a square pulse of depth ΔV_P, it was pulsed into Coulomb blockade to point M, where a microwave burst of duration t_{burst} was applied. Finally, back at the readout point R, a current signal was measured if the spins were in a singlet configuration after manipulation.

Figures 1c,d show typical EDSR measurements, in which the microwave frequency (f_{MW}) was swept versus the applied magnetic field $\mathbf{B}_{ext}$ along the x and y axes, respectively. On resonance, the spin was rotated, which lifted the spin blockade and led to an increased current. From Fig. 1c,d, we extracted $g_x = 1.06$ and $g_y = 1.02$, for the g-factor with $\mathbf{B}_{ext}$ oriented along the x or y axis, respectively. With $\mathbf{B}_{ext}$ aligned along the z direction, no EDSR signal could be observed, as discussed later.

Coherent manipulation and two-axis control

To demonstrate coherent control, we varied the pulse duration t_{burst} and observed Rabi oscillations in the form of a typical chevron pattern (Fig. 2a). Figure 2b shows the dependence on the microwave power (P_{MW}). From line cuts, we extracted the Rabi frequency f_{Rabi} (Methods), which is shown in Fig. 2c as a function of the microwave amplitude (A_{MW}). The data at low amplitudes are in good agreement with a linear fit (black dashed line in Fig. 2c), as expected theoretically. The saturation behaviour at higher amplitudes probably originated from a smaller effective displacement due to anharmonicity[37,38] in the dot confinement for the particular gate voltage configuration used here, leading to a sublinear dependence on the amplitude A_{MW} of the microwave driving field. Additionally, the strong and tunable SOI in our system could potentially lead to such non-linearities.

In the presence of SOI, the oscillating electric field on gate V_{LP} due to the microwaves gives rise to an oscillating effective magnetic field $\mathbf{B}_{eff}(t)$, with magnitude[25]:

$$B_{eff}(t) = 2B_{ext}\frac{l_{dot}}{l_{so}}\frac{eE_{MW}(t)l_{dot}}{\Delta_{orb}} \quad (1)$$

where e is the elementary charge, $\mathbf{E}_{MW}(t)$ the a.c. electric field in the dot generated by the microwaves, l_{dot} the dot length, $\Delta_{orb} \propto l_{dot}^{-2}m_{eff}^{-1}$ with m_{eff} the effective hole mass, the orbital level splitting, and l_{so}, which we define here as setting the distance a hole has to travel along the nanowire to have its spin flipped due to SOI. This effective field $\mathbf{B}_{eff}$ drives the Rabi oscillations, with Rabi frequency $f_{Rabi} = g_{\parallel}\mu_B B_{eff}(t)/(2h)$, with $g_{\parallel}$ the g-factor along the direction of $\mathbf{B}_{ext}$, and h Planck's constant. From equation (1), we see that B_{eff} scales linearly with B_{ext}. We measured the Rabi frequency for different B_{ext} and plotted the result (Fig. 2d). Despite the relatively large error bars at higher fields due to the inaccuracy of the frequency-dependent microwave power calibration (Supplementary Section 1), the measurement agrees well with a linear dependence of the Rabi frequency on B_{ext}, as expected for SOI-mediated EDSR[25,26].

Next, to characterize the free induction decay, we applied a Ramsey pulse sequence, as depicted in Fig. 2e. A fit to a Gaussian decay yielded the dephasing time $T_2^* = 11 \pm 1$ ns. This value is one order of magnitude smaller than that in comparable hole spin qubit systems[12,31,39]. This may be attributed to low-frequency noise, which could, for instance, be due to gate voltage fluctuations, frequency jitter of the microwave source, charge fluctuators or residual nuclear spin noise. Nevertheless, we could mitigate this to a large extent using a Hahn echo sequence to prolong coherence by a factor of ~25, thus demonstrating an efficient decoupling of the qubit from low-frequency noise. In our measurements, we found no clear indication of decay due to spin relaxation. Indeed, previous experimental[40] and theoretical[18] works found spin relaxation times in Ge/Si nanowires to be in the milliseconds to seconds regime, much longer than can be probed using our pulsing and read-out scheme.

Finally, we used a modified Hahn echo pulse sequence to demonstrate two-axis control. We employed either a π_x or a π_y pulse and varied the phase of the second $\pi_\varphi/2$ pulse (see schematics in Fig. 2e). This resulted in two sets of Ramsey fringes, as shown in Fig. 2f, which are phase-shifted by π. These measurements demonstrate universal, two-axis control of the hole spin qubit.

Spin–orbit switch functionality

The measurements of Fig. 2 establish Ge/Si nanowires as a platform for hole spin qubits. The particular direct Rashba SOI[17,20] provides a unique way to electrically control the qubit via the SOI strength and qubit Zeeman energy[18,19]. This tunability can be exploited to optimize qubit relaxation and dephasing times, as well as the selective coupling of the qubit to EDSR drive fields or microwave resonators[19,41,42]. Here we demonstrated this distinct gate tunability of hole spin qubits in Ge/Si core/shell nanowires by investigating electrical control over the g-factor, Rabi frequency and coherence time.

The gate voltages not only provided the electrostatic confinement, but also constitute a static electric field on the order of tens of

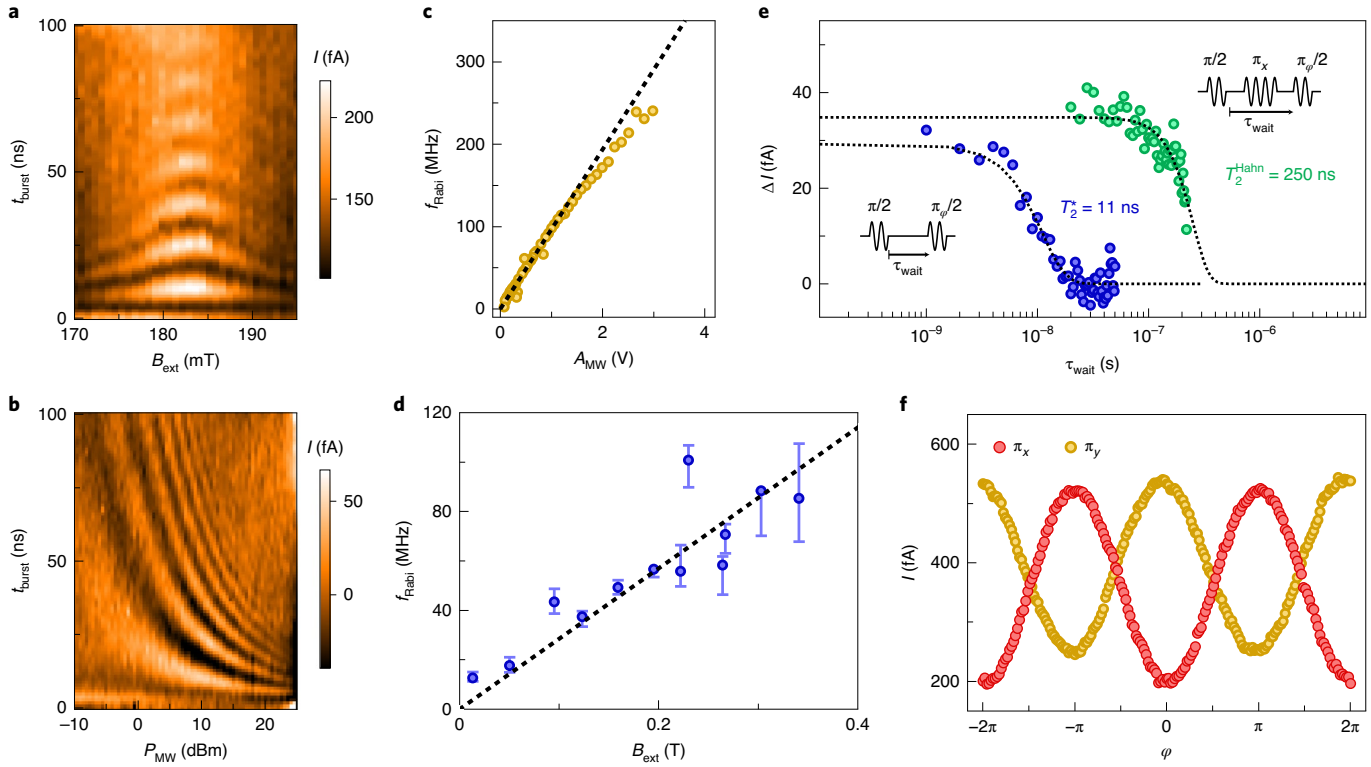

Fig. 2 | Coherent qubit control. a, Measurement of the current as a function of microwave burst duration and magnetic field ($P_{MW} = 10$ dBm). We observed a Rabi frequency of 72 MHz. **b**, Power dependence of Rabi oscillations in the same configuration as in **a** ($B_{ext} = 181$ mT). **c**, Extracted Rabi frequency as a function of A_{MW}, from fits of the data in **b** (see Methods for details). The black dashed line is a linear fit to the extracted Rabi frequencies. **d**, Rabi frequency as a function of the magnitude of the external magnetic field. The black dashed line is a linear fit to the data over the whole range with zero offset. The error bars correspond to the inaccuracy of the frequency-dependent power calibration (Supplementary Section 1). **e**, Decay of Ramsey fringes (blue points) and Hahn echo (green points) as a function of the waiting time τ_{wait} between the two $\pi/2$ pulses. Here ΔI is the difference in current between Ramsey measurements with the second pulse having either $\varphi = 0$ or $\varphi = \pi$. Insets: pulse sequences used for Ramsey fringes (bottom left) and Hahn echo (top right). Black dotted lines are fits of the data to an exponential decay, from which we infer the decay time constants T_*^2 and T_2^{Hahn}, for the Ramsey fringes and Hahn echo, respectively. **f**, Demonstration of two-axis qubit control by applying a Hahn echo sequence with two orthogonal π pulses. The amplitudes of the fringes of the two datasets differ due to an offset in the calibration of the $\pi/2$ pulse duration between the two measurements.

volts per micrometre inside the quantum dots, which has a notable effect on the strength of the SOI[17,20]. Figure 3a shows examples of Rabi oscillations for four different gate voltages V_M. Here, f_{MW} and P_{MW} are kept fixed, while B_{ext} is adjusted to compensate for changes in $g_\parallel$ keeping the qubit on resonance with the microwave drive. As shown in Fig. 3b, we found that the Rabi frequency depended strongly on V_M, and a gate voltage change of 30 mV resulted in a sevenfold increase of the Rabi frequency.

For SOI-mediated spin rotations[25], the Rabi frequency is proportional to the effective magnetic field given by equation (1) and the g-factor $g_\parallel$. For measurements at a fixed microwave frequency f_{MW}, as done here, the apparent g-factor dependence vanishes and the Rabi frequency depends only on the spin-orbit length l_{so}, the quantum dot confinement Δ_{orb}, and the ac electric field $E_{MW}(t)$ created through the periodic gate voltage modulation (see Supplementary equation 1).

We carefully analysed each of the contributions to the change of the Rabi frequency (Supplementary Section 2.2). In particular, we found that the orbital level splitting Δ_{orb} showed only a weak dependence on gate voltage V_M and that the electric field amplitude E_{MW} stayed roughly constant. These effects are not sufficient to explain the large change in f_{Rabi} and therefore the large change must mostly be attributed to a gate tunability of l_{so}. Using equation (1), we extracted upper bounds of l_{so} (Supplementary Section 2.2.1). We found remarkably short values of l_{so} that were tuned from 23 nm down to 4 nm. Here we assumed a heavy-hole effective mass, as suggested by independent transport measurements at high magnetic field[43]. Such a strong SOI has been predicted for the direct Rashba SOI[17,20]. This range of l_{so} overlaps with values found in anti-localization[44] and spin-blockade experiments[43]. Finally, although the direct Rashba SOI term is predicted to be very strong in this system, additional weaker SOI terms may also be present, but cannot be distinguished here.

Besides the Rabi frequency, the coherence was also strongly affected by V_M, as shown in Fig. 3d. We plotted the characteristic driven decay time T_2^{Rabi} (Fig. 3d), and found that it scaled roughly inversely with f_{Rabi} and $g_\parallel$: a short decay time coincides with a high Rabi frequency, and vice versa. Together with the tunability of the Rabi frequency, this control over the qubit coherence time allowed us to define (Fig. 3b,d, insets) a fast qubit manipulation point (control) and a qubit idling point that featured a considerably improved coherence (idle). This demonstrates the functionality of a spin–orbit switch, although here with modest on/off ratios for the switching of f_{Rabi} and T_2^{Rabi} between the control and idle points.

Moreover, the variation of $g_\parallel$ (ref. [45]) in Fig. 3c effectively adds a third mode of operation to the spin–orbit switch, in which individual qubits can be selectively tuned, for instance, in and out of resonance with a microwave cavity, which enables a switch for qubit–resonator coupling[41,42]. Finally, we found that the pulse depth ΔV_P can also be used to tune f_{Rabi} and $g_\parallel$ (Supplementary Section 2.1), which indicates that dynamically pulsing these quantities is feasible.

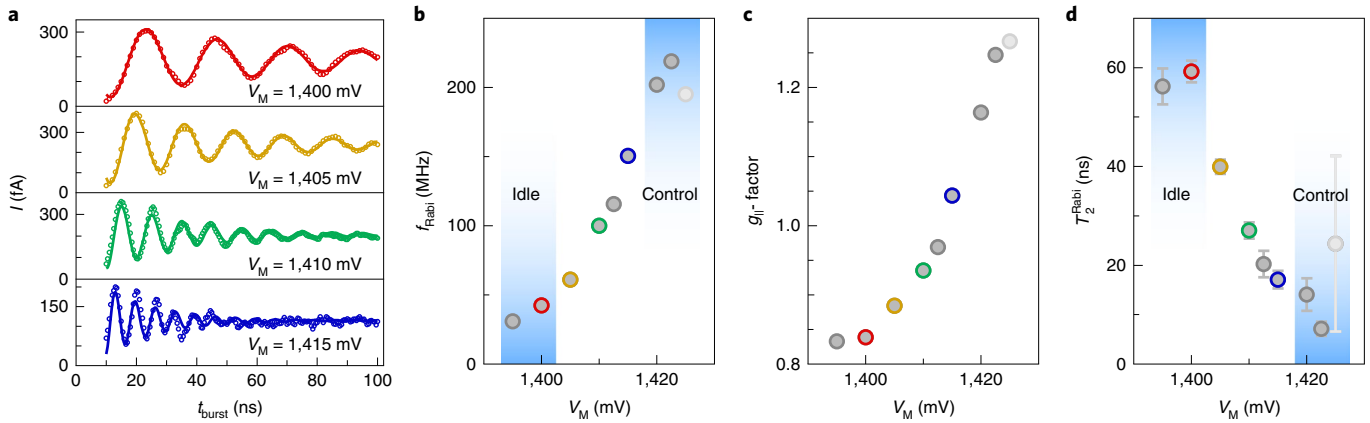

Fig. 3 | Electrical tunability of qubit parameters. a, Rabi oscillations for four different gate voltage values V_M. **b**–**d**, Rabi frequency (**b**), *g*-factor (f_{MW} = 3.4 GHz) (**c**) and T_2^{Rabi} (**d**) as a function of the gate voltage V_M, as extracted from fits to line cuts, such as those shown in **a**. Error bars correspond to the standard deviations that result from the fitting. Insets (**b**,**d**): possible idling and control points. These points define a spin–orbit switch with on/off ratios of 7.1 and 8.3 for f_{Rabi} and T_2^{Rabi}, respectively. Note that the measurement that corresponds to the point at V_M = 1,425 mV (light grey) suffers from a low signal-to-noise ratio, due to a reduced interdot tunnel coupling, which results in a large uncertainty in the analysis of the data at this point.

Ultrafast Rabi oscillations

In a next step, we used the electrical tunability to optimize the gate voltages for a high Rabi frequency and furthermore increased the applied P_{MW}. In Fig. 4, we show a measurement of ultrafast Rabi oscillations, in which the maximum Rabi frequency reaches a value of ~435 MHz (Fig. 4b), which allows for spin-flip times of the qubit as short as 1.15 ns. As can be seen in Fig. 4c, the Rabi frequency scales linearly with applied A_{MW} in this regime of ultrafast qubit operation and shows no signs of saturation for the gate configuration used here, in contrast to that in Fig. 2b. This indicates that even higher Rabi frequencies may be possible through the application of a higher P_{MW}. Note that pulse imperfections play a larger role for a shorter pulse duration and higher amplitudes, which probably partially explains the decrease in T_2^{Rabi} with increasing A_{MW}.

Notably, the observed Rabi frequencies of over 400 MHz are roughly one-eighth of the Larmor precession frequency of 3.4 GHz. The system thus approaches the strong driving regime in which the rotating wave approximation is not applicable anymore, which opens the possibility for ultrafast, non-sinusoidal spin flipping[46,47] that has not been realized before with conventional spin qubits. We note that in our experiment, the effects of strong driving[47] could contribute to the reduced visibility of Rabi oscillations at the high Rabi frequencies shown in Fig. 4.

Conclusions

We have demonstrated ultrafast two-axis control via EDSR of a hole spin qubit in a Ge/Si core/shell nanowire. Our measurements firmly demonstrate the feasibility of single-spin qubit operations on nanosecond timescales. Ideally, such fast operations would be combined with long qubit coherence times. We observed a relatively short inhomogeneous dephasing time, which is probably related to technical pulsing challenges at such short timescales. This may be resolved with improved instrument control. Also, we measured a much larger spin echo decay time, which indicates the presence of low-frequency noise that affects our qubit. Finally, the use of a charge sensor will allow us to decouple the quantum dots from the neighbouring Fermi reservoirs, which could lead to a substantial further enhancement of the coherence time.

We have demonstrated a sevenfold increase of the Rabi frequency for a relatively small change in gate voltage. Similarly, we found that the driven decay time of our qubit can be tuned by the same gate voltage, which demonstrates the working principle of a spin–orbit switch. Thus far, the spin–orbit switch is limited to moderate on/off ratios of f_{Rabi} and T_2^{Rabi}. However, improved devices with gates designed for precise engineering of the electric field profile could, in future experiments, lead to a higher level of control over the SOI, and result in higher on/off ratios as suggested by theoretical work[19]. Our measurements indicate the presence of an exceptionally strong SOI in Ge/Si core/shell nanowires, in qualitative agreement with predictions of a direct Rashba SOI[17,20]. A more quantitative comparison with theory, as well as improved gate switching, requires precise engineering of the electric field and single-hole dot occupation, both of which can be achieved through optimization of the gate design.

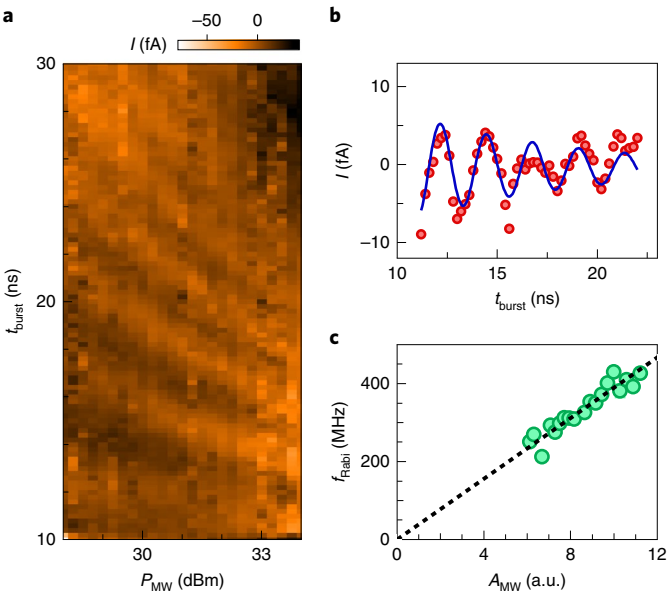

Fig. 4 | Ultrafast coherent control. a, Power dependence of ultrafast Rabi oscillations (f_{MW} = 3.4 GHz, B_y = 206 mT). **b**, Line cut of data shown in **a** at a P_{MW} of 34 dBm (f_{Rabi} = 435 ± 5 MHz). The data are fitted (blue solid curve) as in Fig. 2, after subtraction of a linear background. **c**, Rabi frequency as a function of A_{MW}, extracted from fits to line cuts in **a**. The dashed black line is a linear fit to the data. a.u., arbitrary units.

The high tunability of the qubit demonstrates the suitability of the platform for the implementation of a qubit with switchable interaction strengths. The effect of the gate voltages and the pulse depth on the qubit resonance frequency and the Rabi frequency have the potential to dynamically pulse the characteristic qubit parameters and interaction strengths from a qubit manipulation to an idling point. Furthermore, the spin–orbit switch could allow tuning to 'sweet spots' of operation, where the SOI strength is to first order insensitive to charge noise, leading to enhancement of qubit coherence[20]. Finally, the strong SOI holds potential to realize fast entangling operations between distant spin qubits, mediated by a microwave resonator[19,32,41,42,48].

Online content

Any methods, additional references, Nature Research reporting summaries, source data, extended data, supplementary information, acknowledgements, peer review information; details of author contributions and competing interests; and statements of data and code availability are available at https://doi.org/10.1038/s41565-020-00828-6.

Received: 19 July 2020; Accepted: 30 November 2020;
Published online: 11 January 2021

References

1. Zwanenburg, F. A. et al. Silicon quantum electronics. *Rev. Mod. Phys.* **85**, 961–1019 (2013).
2. Kloeffel, C. & Loss, D. Prospects for spin-based quantum computing in quantum dots. *Annu. Rev. Condens. Matter Phys.* **4**, 51–81 (2013).
3. Vandersypen, L. M. K. et al. Interfacing spin qubits in quantum dots and donors: hot, dense, and coherent. *npj Quantum Inf.* **3**, 34 (2017).
4. Scappucci, G. et al. The germanium quantum information route. Preprint at https://arxiv.org/abs/2004.08133 (2020).
5. Tyryshkin, A. M. et al. Electron spin coherence exceeding seconds in high-purity silicon. *Nat. Mater.* **11**, 143–147 (2012).
6. Yoneda, J. et al. A quantum-dot spin qubit with coherence limited by charge noise and fidelity higher than 99.9%. *Nat. Nanotechnol.* **13**, 102–106 (2018).
7. Kawakami, E. et al. Electrical control of a long-lived spin qubit in a Si/SiGe quantum dot. *Nat. Nanotechnol.* **9**, 666–670 (2014).
8. Veldhorst, M. et al. An addressable quantum dot qubit with fault-tolerant control-fidelity. *Nat. Nanotechnol.* **9**, 981–985 (2014).
9. Veldhorst, M. et al. A two-qubit logic gate in silicon. *Nature* **526**, 410–414 (2015).
10. Zajac, D. M. et al. Resonantly driven CNOT gate for electron spins. *Science* **359**, 439–442 (2018).
11. Watson, T. F. et al. A programmable two-qubit quantum processor in silicon. *Nature* **555**, 633–637 (2018).
12. Hendrickx, N. W., Franke, D. P., Sammak, A., Scappucci, G. & Veldhorst, M. Fast two-qubit logic with holes in germanium. *Nature* **577**, 487–491 (2020).
13. Loss, D. & DiVincenzo, D. P. Quantum computation with quantum dots. *Phys. Rev. A* **57**, 120–126 (1998).
14. Bulaev, D. V. & Loss, D. Spin relaxation and decoherence of holes in quantum dots. *Phys. Rev. Lett.* **95**, 076805 (2005).
15. Maurand, R. et al. CMOS silicon spin qubit. *Nat. Commun.* **7**, 13575 (2016).
16. Crippa, A. et al. Gate-reflectometry dispersive readout and coherent control of a spin qubit in silicon. *Nat. Commun.* **10**, 2776 (2019).
17. Kloeffel, C., Trif, M. & Loss, D. Strong spin–orbit interaction and helical hole states in Ge/Si nanowires. *Phys. Rev. B* **84**, 195314 (2011).
18. Maier, F., Kloeffel, C. & Loss, D. Tunable *g*-factor and phonon-mediated hole spin relaxation in Ge/Si nanowire quantum dots. *Phys. Rev. B* **87**, 161305 (2013).
19. Kloeffel, C., Trif, M., Stano, P. & Loss, D. Circuit QED with hole-spin qubits in Ge/Si nanowire quantum dots. *Phys. Rev. B* **88**, 241405 (2013).
20. Kloeffel, C., Rančić, M. J. & Loss, D. Direct Rashba spin–orbit interaction in Si and Ge nanowires with different growth directions. *Phys. Rev. B.* **97**, 235422 (2018).
21. Yang, C. H. et al. Spin-valley lifetimes in a silicon quantum dot with tunable valley splitting. *Nat. Commun.* **4**, 2069 (2013).
22. Prechtel, J. H. et al. Decoupling a hole spin qubit from the nuclear spins. *Nat. Mater.* **15**, 981–986 (2016).
23. Durnev, M. V., Glazov, M. M. & Ivchenko, E. L. Spin–orbit splitting of valence subbands in semiconductor nanostructures. *Phys. Rev. B* **89**, 075430 (2014).
24. Marcellina, E., Hamilton, A. R., Winkler, R. & Culcer, D. Spin–orbit interactions in inversion-asymmetric two-dimensional hole systems: a variational analysis. *Phys. Rev. B* **95**, 075305 (2019).
25. Golovach, V. N., Borhani, M. & Loss, D. Electric-dipole-induced spin resonance in quantum dots. *Phys. Rev. B* **74**, 165319 (2006).
26. Nowack, K. C., Koppens, F. H. L., Nazarov, Y. V. & Vandersypen, L. M. K. Coherent control of a single electron spin with electric fields. *Science* **318**, 1430–1433 (2007).
27. Bulaev, D. V. & Loss, D. Electric dipole spin resonance for heavy holes in quantum dots. *Phys. Rev. Lett.* **98**, 097202 (2007).
28. van den Berg et al. Fast spin-orbit qubit in an indium antimonide nanowire. *Phys. Rev. Lett.* **110**, 066806 (2013).
29. Pioro-Ladriere, M. et al. Electrically driven single-electron spin resonance in a slanting Zeeman field. *Nat. Phys.* **4**, 776–779 (2008).
30. Koppens, F. H. L. et al. Driven coherent oscillations of a single electron spin in a quantum dot. *Nature* **442**, 766–771 (2006).
31. Watzinger, H. et al. A germanium hole spin qubit. *Nat. Commun.* **9**, 3902 (2018).
32. Burkard, G., Gullans, M. J., Mi, X. & Petta, J. R. Superconductor–semiconductor hybrid-circuit quantum electrodynamics. *Nat. Rev. Phys.* **2**, 129–140 (2020).
33. Brauns, M., Ridderbos, J., Li, A., Bakkers, E. P. A. M. & Zwanenburg, F. A. Highly tuneable hole quantum dots in Ge–Si core-shell nanowires. *Appl. Phys. Lett.* **109**, 143113 (2016).
34. Conesa-Boj, S. et al. Boosting hole mobility in coherently strained [110]-oriented Ge–Si core–shell nanowires. *Nano Lett.* **17**, 2259–2264 (2017).
35. Froning, F. N. M. et al. Single, double, and triple quantum dots in Ge/Si nanowires. *Appl. Phys. Lett.* **113**, 073102 (2018).
36. Ono, K., Austing, D. G., Tokura, Y. & Tarucha, S. Current rectification by Pauli exclusion in a weakly coupled double quantum dot system. *Science* **297**, 1313–1317 (2002).
37. Yoneda, J. et al. Fast electrical control of single electron spins in quantum dots with vanishing influence from nuclear spins. *Phys. Rev. Lett.* **113**, 267601 (2014).
38. Takeda, K. et al. S. A fault-tolerant addressable spin qubit in a natural silicon quantum dot. *Sci. Adv.* **2**, e1600694 (2016).
39. Higginbotham, A. P. et al. Hole spin coherence in a Ge/Si heterostructure nanowire. *Nano Lett.* **14**, 3582–3586 (2014).
40. Hu, Y., Kuemmeth, F., Lieber, C. M. & Marcus, C. M. Hole spin relaxation in Ge–Si core–shell nanowire qubits. *Nat. Nanotechnol.* **7**, 47–50 (2012).
41. Trif, M., Golovach, V. N. & Loss, D. Spin dynamics in InAs nanowire quantum dots coupled to a transmission line. *Phys. Rev. B* **77**, 045434 (2008).
42. Nigg, S. E., Fuhrer, A. & Loss, D. Superconducting grid-bus surface code architecture for hole-spin qubits. *Phys. Rev. Lett.* **118**, 147701 (2017).
43. Froning, F. N. M. et al. Strong spin–orbit interaction and *g*-factor renormalization of hole spins in Ge/Si nanowire quantum dots. Preprint at https://arxiv.org/abs/2007.04308 (2020).
44. Higginbotham, A. P. et al. Antilocalization of coulomb blockade in a Ge/Si nanowire. *Phys. Rev. Lett.* **112**, 216806 (2014).
45. Dmytruk, O., Chevallier, D., Loss, D. & Klinovaja, J. Renormalization of the quantum dot *g*-factor in superconducting Rashba nanowires. *Phys. Rev. B* **98**, 165403 (2018).
46. Kato, Y. et al. Gigahertz electron spin manipulation using voltage-controlled *g*-tensor modulation. *Science* **299**, 1201–1204 (2003).
47. Laucht, A. et al. Breaking the rotating wave approximation for a strongly driven dressed single-electron spin. *Phys. Rev. B* **94**, 161302 (2016).
48. Borjans, F., Croot, X. G., Mi, X., Gullans, M. J. & Petta, J. R. Resonant microwave-mediated interactions between distant electron spins. *Nature* **577**, 195198 (2020).

Methods

Device fabrication. The device featured a set of five gates with a width of 20 nm and a pitch of 50 nm defined by electron beam lithography on a p^{++}-doped Si chip covered with 290 nm of thermal oxide. The gates were covered by a 20-nm-thick layer of Al_2O_3 grown by atomic layer deposition to electrically insulate them from the nanowire. A single Ge/Si core/shell nanowire with a core radius of about 10 nm and a shell thickness of 2.5 nm (ref. [34]) was placed deterministically across the set of gates using a micromanipulator. The nanowire was roughly aligned with the coordinate system in Fig. 1b, but the exact angle in the x–z plane is unknown. Finally, ohmic contacts were fabricated by electron beam lithography and metallized with Ti/Pd following a short dip in hydrofluoric acid to remove the native oxide. The scanning electron micrograph shown in Fig. 1a is from a similarly fabricated device as described here.

Experimental set-up. The sample was wire bonded to a printed-circuit board that provided d.c. wiring and radiofrequency lines, coupled via bias tees. The circuit board was mounted in a Bluefors dilution refrigerator with a base temperature around 10 mK, at which temperature all the measurements were taken. Each high-frequency line included attenuators with combined values of ~30 dB. A Basel Precision Instruments LNHR DAC was used to supply the d.c. voltages, and a Basel Precision Instruments LNHS I/V converter was used for the readout of the qubit in transport.

A Tektronix 7122C or AWG5208 arbitrary waveform generator was used to generate the square voltage pulses applied to gate V_{LP}. To drive the qubit, either an analogue Keysight E8257D signal generator or an E8267D vector signal generator supplied the microwave tone. For measurements at high P_{MW}, an RF-Lambda model RFQ132070 amplifier was used. Two different configurations of the set-up were used for the microwave burst generation. For the measurements shown in Figs. 1c,d, 2d, 3 and 4, the amplitude of the microwaves was modulated by means of an RF switch (ZASWA-2-50DRA+; MiniCircuits), triggered by the arbitrary waveform generator. The RF switch has a minimum pulse width of 10 ns. For the measurements shown in Figs. 1b and 2a–c,e,f, the microwave bursts were generated by IQ modulation of the vector signal generator's microwave tone. Here, the minimum pulse width was 6 ns. In either configuration, a lock-in amplifier was used to chop the bursted microwaves at a frequency of 89.75 Hz and the I/V converter output was demodulated at this frequency. This allowed us to separate the current signal due to the applied microwaves from the background.

Data analysis. Rabi frequencies were extracted from fits to $I(t_{\mathrm{burst}}) = I_0 + C\sin(2\pi f_{\mathrm{Rabi}} t_{\mathrm{burst}} + \phi)\exp(-t_{\mathrm{burst}}/T_2^{\mathrm{Rabi}})$. Here, I_0 is an offset, C the amplitude, ϕ a phase shift and T_2^{Rabi} the characteristic decay time. Furthermore, we post-processed raw datasets in the following ways. The data in Fig. 1c (1d) was offset by 10 mT (20 mT) to compensate for the trapped magnetic flux. Furthermore, the average value was subtracted from each column and row of the raw data. Then, each row was divided by the average row value. Similarly, for the data in Figs. 2b and 4a, the average value was subtracted from each column and row of the raw data. In Fig. 4a, the data for microwave burst times below the minimum pulse width achievable by our electronics are omitted.

Measurement details. In the following we list the relevant parameters that were used for the various measurements. For the measurements in Fig. 1c,d, a fixed pulse amplitude $\Delta V_P = 0.55$ V and a burst duration $t_{\mathrm{burst}} = 15$ ns were used. In Fig. 2a–c, B_{ext} was oriented along the $-y$ axis. For Fig. 2d, $f_{MW} = 3.4$ GHz was used and B_{ext} was oriented in the x–y plane, at an angle of 40° to the y axis. In Fig. 2e, the duration of the π pulse was $t_\pi = 13$ ns, $P_{MW} = 3$ dBm, $f_{MW} = 2.6$ GHz, and $B_{\mathrm{ext}} = 181$ mT along the $-x$ axis. For Fig. 2f, we used $P_{MW} = 14$ dBm, $f_{MW} = 3.4$ GHz and $B_{\mathrm{ext}} = 292$ mT, along the same direction as used for Fig. 2d. Finally, for the measurements of Fig. 3, we used $P_{MW} = 25$ dBm and the orientation of $\mathbf{B}_{\mathrm{ext}}$ was the same as that in Fig. 2d.

For completeness, we also mention the other gate voltages used for the measurements in Fig. 3: $V_L = 3{,}710$ mV and $V_R = 1{,}495$ mV; V_{LP} and V_{RP} depend on V_M, but are similar to the values used for Fig. 1b.

Data availability

The data supporting the plots of this paper are available at the Zenodo repository at https://doi.org/10.5281/zenodo.4290131.

Acknowledgements

We thank S. Bosco, B. Hetényi, C. Kloeffel, D. Loss, A. Laucht and A. Hamilton for useful discussions. Furthermore, we acknowledge S. Martin and M. Steinacher for technical support. This work was partially supported by the Swiss Nanoscience Institute (SNI), the NCCR QSIT, the NCCR SPIN, the Georg H. Endress Foundation, Swiss NSF (grant no. 179024), the EU H2020 European Microkelvin Platform EMP (grant no. 824109) and FET TOPSQUAD (grant no. 862046).

Author contributions

F.N.M.F., L.C.C., F.R.B. and D.M.Z. conceived the project and experiments. F.N.M.F. fabricated the device. A.L. and E.P.A.M.B. synthesized the nanowire. F.N.M.F., L.C.C., O.A.H.v.d.M., F.R.B. and D.M.Z. performed the experiments. F.N.M.F., L.C.C., F.R.B. and D.M.Z. analysed the measurements and wrote the manuscript with input from all the authors.

Competing interests

The authors declare no competing interests.

Additional information

Supplementary information is available for this paper at https://doi.org/10.1038/s41565-020-00828-6.

Correspondence and requests for materials should be addressed to D.M.Z. or F.R.B.

Peer review information *Nature Nanotechnology* thanks the anonymous reviewers for their contribution to the peer review of this work.

Reprints and permissions information is available at www.nature.com/reprints.